Magneto-optical detection of topological contributions to the anomalous Hall effect in a kagome ferromagnet

F. Schilberth [1,2,*] N. Unglert,[3,*] L. Prodan,[1] F. Meggle,[4] J. Ebad Allah,[4] C. A. Kuntscher,[4] A. A. Tsirlin,[5]
V. Tsurkan,[1,6] J. Deisenhofer,[1] L. Chioncel,[3] I. Kézsmárki,[1] and S. Bordács[2]

[1]*Experimentalphysik V, Center for Electronic Correlations and Magnetism, Institute for Physics,
Augsburg University, D-86135 Augsburg, Germany*
[2]*Department of Physics, Institute of Physics, Budapest University of Technology and Economics,
Műegyetem rakpart 3., H-1111 Budapest, Hungary*
[3]*Theoretische Physik III, Center for Electronic Correlations and Magnetism, Institute for Physics,
Augsburg University, D-86135 Augsburg, Germany*
[4]*Experimentalphysik II, Institute for Physics, Augsburg University, D-86135 Augsburg, Germany*
[5]*Experimentalphysik VI, Center for Electronic Correlations and Magnetism, Institute for Physics,
Augsburg University, D-86135 Augsburg, Germany*
[6]*Institute of Applied Physics, MD-2028 Chişinău, Republic of Moldova*

A single ferromagnetic kagome layer is predicted to realize a Chern insulator with quantized Hall conductance, which upon stacking can become a Weyl semimetal with a large anomalous Hall effect (AHE) and magneto-optical activity. Indeed, in the kagome bilayer material Fe_3Sn_2, a large AHE was detected. In order to directly probe the responsible band structure features, we measure the optical Hall conductivity spectra in addition to the diagonal optical conductivity over a broad frequency range. Since the former is the energy selective measure of the intrinsic contributions to the AHE, we identify their common origin with the help of momentum- and band-decomposed optical conductivity spectra obtained from first principles calculations. We find that low-energy transitions, tracing "helical volumes" in momentum space reminiscent of the formerly predicted helical nodal lines, substantially contribute to the AHE, which is further increased by contributions from multiple higher-energy interband transitions. Our study also reveals that in this kagome magnet, local Coulomb interactions lead to remarkable band reconstructions near the Fermi level.

I. INTRODUCTION

Recently, much effort has been focused on the study of materials derived from the kagome lattice—the triangular lattice of corner-sharing triangles—as they realize flat bands [1–4] and Dirac fermions [4–6]. Symmetry breaking phase transitions often give rise to topologically nontrivial electronic states in these compounds: magnetic Weyl semimetals [7,8], magnetic skyrmions [9,10], and unconventional superconductivity [3,11–15].

One of the most profound manifestations of the interplay between magnetism and the topology of the itinerant electrons is the intrinsic anomalous Hall effect (AHE) [16]. If the spin degeneracy of the electronic bands is lifted by breaking the time-reversal symmetry, their spin-orbit mixing leads to a finite Berry curvature, which, as a fictitious magnetic field, deflects electric currents [17]. Remarkably, the AHE can become quantized in two dimensions (2D) by tuning the Fermi energy into the exchange gap between topologically nontrivial bands, as suggested for the case of a single kagome layer [18]. When such layers are stacked in 3D, a magnetic Weyl semimetal showing an enhanced AHE response can be realized [6,19].

Recently, a large AHE was observed in the kagome bilayer compound Fe_3Sn_2 [5,20]. The temperature-independent response, assumed to represent the intrinsic AHE, was attributed to the Dirac(-like) quasiparticles emerging in the vicinity of the K point. However, optical spectroscopy and scanning tunneling microscopy (STM) studies also indicate the presence of flat bands close to the Fermi energy [21,22]. Therefore, the direct assignment of the bands responsible for the large intrinsic AHE is still an open issue.

Fe_3Sn_2 (space group $R\bar{3}m$) consists of an alternating stack of Fe_3Sn kagome bilayers and honeycomb layers of Sn, as shown in the inset of Fig. 1(c) [23]. A ferromagnetic order develops below $T_c = 657$ K. The moments are aligned along the c axis at high temperature and they gradually rotate toward the ab plane as the temperature is lowered [9,23,24]. Whether the ferromagnetic order in bulk Fe_3Sn_2 is completely collinear is under debate, while in thin samples the combination of the ferromagnetic exchange, the easy-axis anisotropy, and the dipolar interactions lead to branched domains and even skyrmionic bubbles [9,24–26]. Owing to the kagome structure, Fe_3Sn_2 shows nontrivial electronic topology. The presence of Weyl nodes in the 10 meV vicinity of
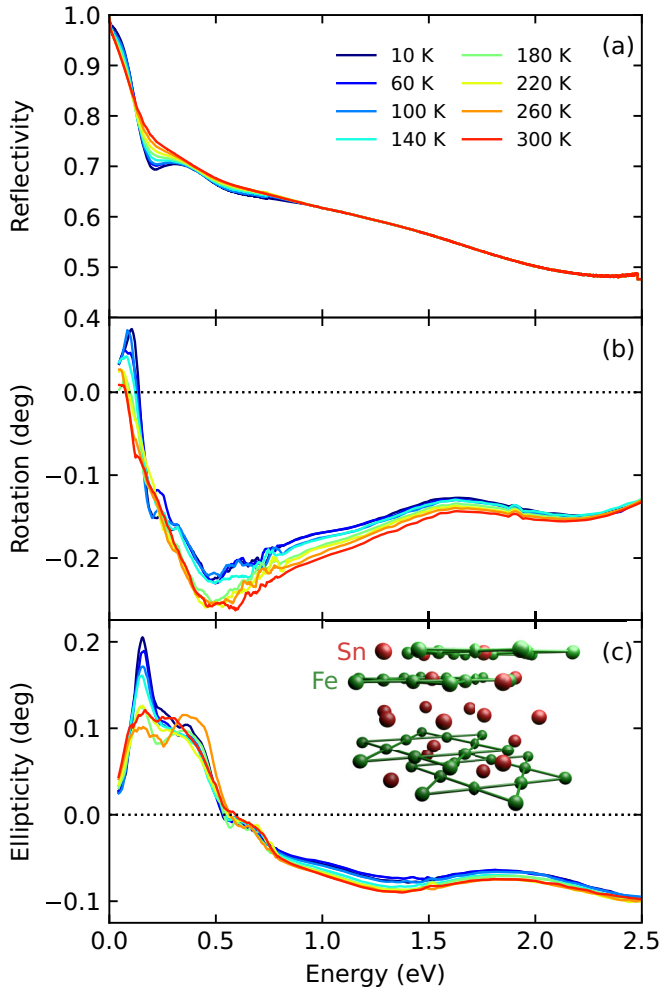
FIG. 1. Spectra measured for several temperatures between 10 and 300 K of (a) the reflectivity, (b) Kerr rotation, and (c) ellipticity in the energy range up to 2.5 eV. The inset in (c) shows a structural unit highlighting the stacking order.

the Fermi energy [27], several Dirac nodes at the K points [5,21,28–30], as well as flat electron bands [21,31] have been proposed.

Identifying whether these features are the main source of the AHE is difficult based on magnetotransport experiments alone, since the response is a sum of the intrinsic and extrinsic contributions with a sometimes identical dependence on the longitudinal conductivity [16]. Due to its energy-resolved nature, the off-diagonal or optical Hall conductivity spectrum $\sigma_{xy}(\omega)$ can provide the necessary information to identify the interband transitions contributing to the intrinsic AHE, as demonstrated for the nearly half-metallic $CuCr_2Se_4$ and Weyl semimetal candidates $SrRuO_3$ and $Co_3Sn_2S_2$ [17,32–34]. Besides providing guidance for the assignment of interband transitions, the theoretical modeling based on the density functional theory (DFT) [35–37] is frequently used to characterize topological features [38] mostly based on the results of band-structure calculations or associated Berry phases [39].

In this paper, we report a broadband magneto-optical study of both the diagonal and Hall conductivity spectra in Fe_3Sn_2 over the energy range 50 meV–2.5 eV. Compared

to angle-resolved photoemission spectroscopy (ARPES), this technique probes the bulk electronic states via the transition matrix elements directly related to AHE. We observed a noticeably high $\sigma_{xy}(\omega)$ with distinct features in the infrared range, where the magneto-optical effects show a strong temperature dependence. At the low-energy cutoff of our measurements, the real part of $\sigma_{xy}(\omega)$ closely approaches the dc value of the AHE, implying that our study covers all relevant interband transitions for the intrinsic contribution. We identified three excitation continua in $\sigma_{xy}(\omega)$ yielding the main contributions to the static Hall effect. *Ab initio* calculations allowed us to identify the bands governing the intrinsic AHE and locate the hot spots in the Brillouin zone which dominate the diagonal and off-diagonal optical conductivity. Our study sheds light on the striking electronic features arising from the kagome units.

II. EXPERIMENTAL METHODS

The broadband reflectivity and near normal incidence magneto-optical Kerr effect (MOKE) spectra were measured on the as-grown *ab* surface of single crystals with a lateral size of ~3 mm. The latter was measured in ±0.3 T to determine the complex magneto-optical Kerr rotation, which is antisymmetric in the magnetic field. The diagonal optical conductivity spectrum was obtained by Kramers-Kronig transformation of the reflectivity, measured over the range of 0.01–2.5 eV. The Hall conductivity spectra were calculated using the complex Kerr rotation (0.05–2.5 eV) according to

$$\theta(\omega) + i\eta(\omega) = -\frac{\sigma_{xy}(\omega)}{\sigma_{xx}(\omega)\sqrt{1 + i\frac{1}{\varepsilon_0\omega}\sigma_{xx}(\omega)}}, \quad (1)$$

where ω is the angular frequency of the photon, $\sigma_{xx}(\omega)$ is the optical conductivity spectrum, ϵ_0 is the vacuum permittivity, and $\theta(\omega)$ and $\eta(\omega)$ are the Kerr rotation and ellipticity, respectively (for details see Supplemental Material [40]).

III. EXPERIMENTAL RESULTS

We present the reflectivity and MOKE spectra measured at several temperatures from 10 to 300 K in Fig. 1. In agreement with former results [21], the reflectivity shows metallic behavior (for log-lin scale compare Fig. S1 [40]): Towards zero frequency it approaches unity and at 0.125 eV, it drops corresponding to the plasma edge, that becomes sharper toward low temperatures. Since the magnetic order in Fe_3Sn_2 develops well above the studied temperature range, we detected a finite Kerr effect already at room temperature. The simultaneously measured rotation and ellipticity spectra can be closely mapped on each other by Kramers-Kronig transformation, validating the measurement procedure. Accompanying the plasma edge, the rotation spectra show a steep increase whereas the ellipticity has a peak which becomes more pronounced toward low temperatures. The dielectric response appearing in the denominator in Eq. (1) is strongly suppressed at the plasma frequency and correspondingly enhances the MOKE [41]. Around 0.5 eV, the rotation exhibits a broad minimum and the ellipticity shows a zero crossing. At higher energies, both Kerr parameters remain negative with
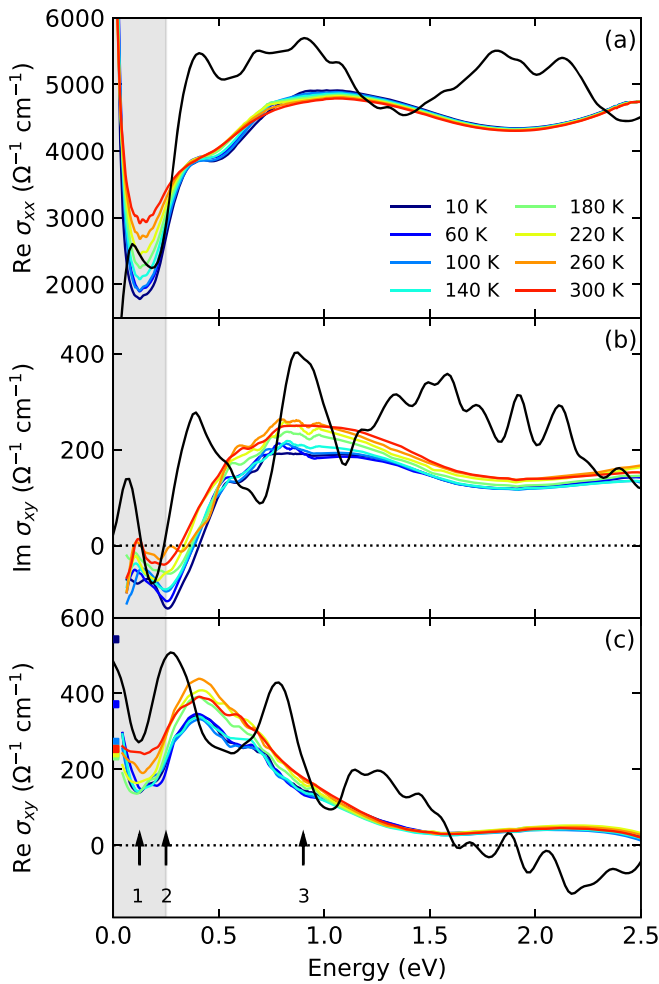
FIG. 2. Comparison of the experimental conductivity spectra measured between 10 and 300 K (colored lines) and the theoretical DFT spectra (black lines) calculated as described in the text. (a)–(c) respectively show the real part of the diagonal, Re σ_{xx}, as well as the imaginary and real part of the off-diagonal conductivity spectra Im σ_{xy} and Re σ_{xy}. For Re σ_{xy}, the static AHE values are plotted for comparison.

a small monotonous temperature dependence. Above 0.8 eV, the overlapping interband transitions form a rather featureless optical response. The derived diagonal and the off-diagonal elements of the conductivity tensor are displayed in Fig. 2. In the real part of the diagonal conductivity, Re σ_{xx}, there is a step edge at 0.25 eV and a broad hump centered at 0.9 eV, both located well above the Drude tail. Our diagonal optical conductivity spectrum agrees with that published in Ref. [21]. Figure 2(b) displays the imaginary part of the off-diagonal conductivity corresponding to the absorption difference for left and right circularly polarized photons. Im $\sigma_{xy}(\omega)$ shows three dominant features: a small positive peak at 0.1 eV (1), a minimum at 0.25 eV (2), and a broad hump around 0.9 eV (3), their energies indicated by arrows. The minimum slightly shifts to higher energies toward low temperatures, whereas the magnitude of Im σ_{xy} at higher energies decreases. As expected from the Kramers-Kronig connection between Re and Im σ_{xy}, the derivative shape of these features appears in Re σ_{xy} as
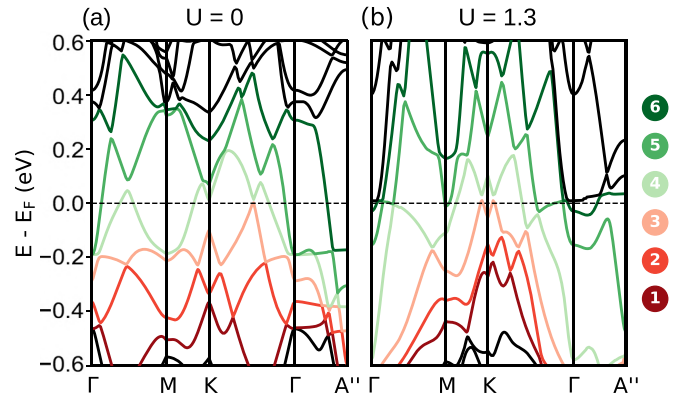

FIG. 3. (a) and (b) show the band structure of Fe_3Sn_2 as determined using GGA+SO without and with $+U$ correction, respectively. Bands relevant for the low-energy transitions are assigned by indices ranging from 1 to 6 and are colored correspondingly. For the assignment of the high-symmetry points, refer to Fig. S6 [40].

shown in Fig. 2(c). For comparison, the dc Hall conductivity values extracted from the measurement in Fig. S2 [40] are included also.

Importantly, at the low-energy cutoff, 0.05 eV, the Re σ_{xy} spectra closely match the corresponding static values, except for temperatures below 100 K, where the increase of the dc AHE is suspected to be caused by enhanced extrinsic contributions [5,20]. This implies that Re σ_{xy} extends smoothly to the dc limit. In other words, our data mainly capture the interband transitions, which govern the intrinsic dc AHE.

IV. CALCULATION OF OPTICAL CONDUCTIVITY

To elucidate the origin of the spectral features, we performed DFT calculations in WIEN2K [42] using a generalized gradient approximation (GGA) functional [43] for the exchange correlation energy and with spin-orbit (SO) coupling introduced in a second variational procedure. Although shown and discussed in several previous publications [27–29,31] we consider first in some detail the electronic structure and the magnetic properties of Fe_3Sn_2. It is well known that DFT (GGA) fails to properly describe the ground state of many systems including relatively narrow d states. In particular, we found that applying the $+U$ corrections significantly improves the agreement between the calculated and measured optical conductivity spectra in Fe_3Sn_2. A detailed comparison for several values of U is provided in Fig. S3 [40], where the best agreement is obtained for 1.3 eV. Consequently, we considered the so-called Hubbard correction $U = 1.3$ eV to Fe(3d) orbitals in the following, and set $J = 0$ for the Hund parameter to ensure that the Fe spin and orbital moments in the ferromagnetic ground state remain of the same magnitude as for $U = 0$, $\mu_{Fe,spin}^{GGA(+U)+SO} = 2.5\mu_B$, and $\mu_{Fe,orb.}^{GGA(+U)+SO} = 0.1\mu_B$, respectively. Note that the same U and J values provide a good agreement between the theoretical and experimental ARPES spectra [44] and is in the range of values used in a different publication [27].

The band structure calculated for $U = 0$, displayed in Fig. 3(a), is in a good agreement with the results reported by Ref. [30], where two helical nodal lines in close vicinity to
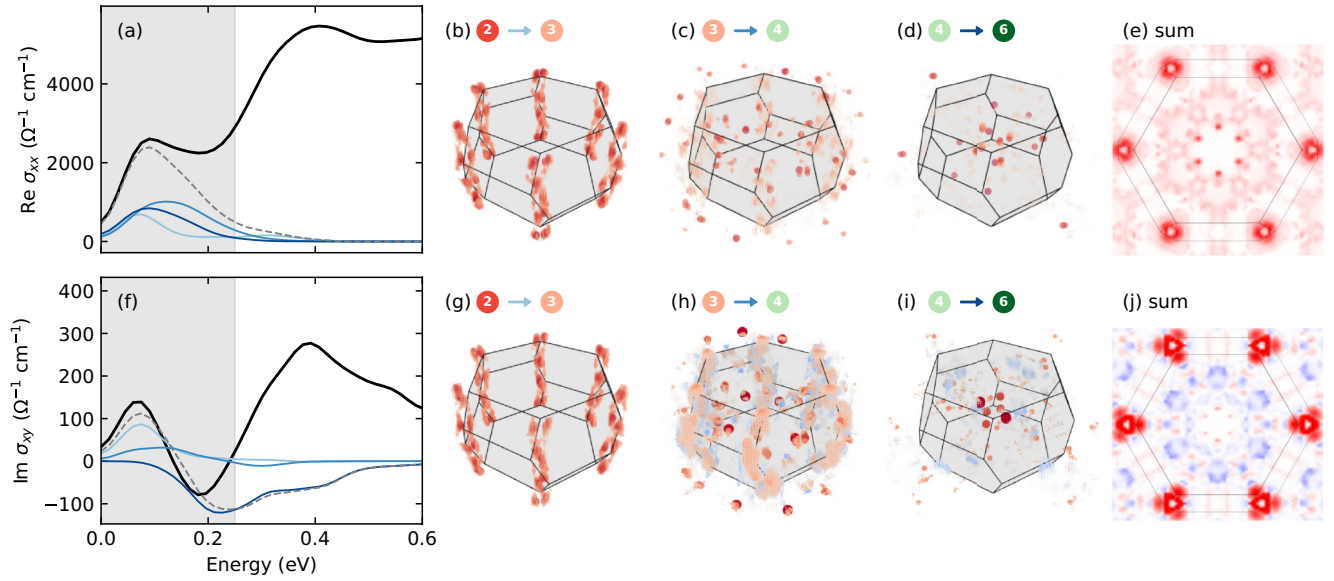
FIG. 4. Decomposition of the calculated spectra into the three transitions ($2 \rightarrow 3$, $3 \rightarrow 4$, and $4 \rightarrow 6$) with maximum spectral weight for the energy window of 0–0.25 eV (shaded in gray). (a)/(f) The total spectrum calculated for Re σ_{xx}/Im σ_{xy} is shown in black, while contributions of the three transitions are plotted in blue shades and their sum in dashed gray. (b)–(d) k-resolved spectral weight distributions $\rho_{\alpha\beta}^{n \rightarrow n'}(\boldsymbol{k}, 0\,\mathrm{eV} < \hbar\omega < 0.25\,\mathrm{eV})$ of the three transitions and their sum (e) for Re σ_{xx}. The numerical labels refer to the bands as in Fig. 3 while the arrows have the same color as the corresponding spectra in (a). (g)–(j) depict the same information for Im σ_{xy}, where k regions with red/blue color represent positive/negative values. As seen in (b) and (g), the lowest-energy transitions are located around the H'-K-H'' line as "helical volumes" and dominate the off-diagonal response around 0.1 eV.

the H'-K-H'' line are identified. The emergence of these nodal lines was attributed to the trigonal stacking of kagome layers and to the rhombohedral symmetry in Fe$_3$Sn$_2$. As expected, the effect of the Hubbard U parameter leads to a reorganization of the energy bands as shown in Fig. 3(b) (for a detailed plot of the band structure for $U = 1.3$ eV, see Fig. S4 [40]). We therefore observed a disruption of the nodal lines (derived from the DFT Hamiltonian computation of Ref. [30]) due to the presence of effective Hubbard interactions. Especially the bands 3 and 4 in Fig. 3(b), forming a double linear avoided crossing at K, are pushed to the Fermi edge by introducing finite U, making them accessible for low-energy optical transitions. This can be traced in the calculated low-energy optical weights in Re σ_{xx} and Im σ_{xy}, displayed in Fig. 4. Similarly strong reconstructions of the bands 2–5 can be followed, e.g., along the Γ-M line. For example, the crossing of bands 2 and 3 for $U = 0$ is dissolved for 1.3 eV. Overall, one clearly sees that the band structure in the 0.5 eV vicinity of the Fermi energy is rather sensitive to the choice of U. Moreover, the observed band reconstruction has a strong and complicated k dependence.

We calculate the dissipative part of the optical spectra, i.e., Re σ_{xx} and Im σ_{xy}, using the Kubo linear response theory [45],

$$\sigma_{\alpha\beta}(\omega) = \frac{4\pi e^2}{m^2\omega^2} \sum_{n,n'} \int d\boldsymbol{k} \langle n\boldsymbol{k}|\hat{p}_\alpha|n'\boldsymbol{k}\rangle \langle n'\boldsymbol{k}|\hat{p}_\beta|n\boldsymbol{k}\rangle$$

$$\times f_{n\boldsymbol{k}}(1 - f_{n'\boldsymbol{k}})\delta(\epsilon_{n\boldsymbol{k}} - \epsilon_{n'\boldsymbol{k}} - \omega), \qquad (2)$$

with $\alpha, \beta = x, y, z$ and $\hat{p}_{\alpha/\beta}$ being the components of the momentum operator; $f_{n\boldsymbol{k}}$ is the Fermi function. Equation (2)

contains the sum over the bands (the band index also includes spin) where only interband ($n \neq n'$) contributions are considered. The theoretical spectrum of the Re σ_{xy} was obtained by a Kramers-Kronig transformation of the imaginary part. For plotting, the spectra are convoluted with a Gaussian with a full width at half maximum (FWHM) of 50 meV.

We present the overall comparison of the theoretical and experimental spectra in Fig. 2. Apart from the intraband (Drude) contributions that are not included in the calculations, the theory correctly captures the low-energy diagonal optical conductivity Re σ_{xx}. Importantly, the calculations reproduce the prominent step edge at 0.25 eV, and they indicate that multiple bands contribute significantly to this feature (see Fig. S5 [40]). The calculated imaginary and real parts of σ_{xy} in Figs. 2(b) and 2(c), respectively, reveal more spectral features that are also in good agreement with the experiments. In Im σ_{xy}, the theory resolves a positive peak at 0.1 eV, a minimum at 0.2 eV, and another positive peak at 0.4 eV that are all present in the experimental data though slightly shifted to higher energies. The peak occurring around 0.9 eV appears in the measurement as a broad plateau centered at the same energy which swallows the surrounding sharper features. Since the theory curves are sharper than the experimental spectra, a larger frequency-independent broadening could improve the overall correspondence, but the low-frequency features would certainly be masked. Although only interband transitions are included in the calculations, the dc extrapolation of theoretical Re σ_{xy} agrees well with the range of measured AHE, which implies largely intrinsic AHE in Fe$_3$Sn$_2$. We emphasize that none of the individual features in Im σ_{xy} discussed above is

responsible for the static Hall effect alone, but their interplay can fully capture the dc AHE.

V. DISCUSSION

Having established the connection between theoretical and experimental spectra, we now investigate the origin of the optical response by band- and k-resolved calculations. It is common practice to split the band summations in Eq. (2) and examine the contributions of individual transitions. Especially for simple systems with a clearly arranged band manifold, this is often sufficient to assign certain observed transitions to features in the electronic structure. However, for complex multiband systems it turns out to be cumbersome to apply this type of analysis. Furthermore, one tends to miss important contributions, arising from regions in reciprocal space which lie off the high-symmetry lines usually employed to visualize the electronic band structure. Therefore, to disentangle the contributions arising from the multitude of bands in Fe_3Sn_2, we performed the analysis of the optical spectra in different photon energy windows, monitoring the spectral density $\rho_{\alpha\beta}^{n\rightarrow n'}(\mathbf{k}, \omega)$ decomposition of the optical conductivity: $\sigma_{\alpha\beta}(\omega) = \sum_{n,n'} \int_{BZ} d\mathbf{k}\, \rho_{\alpha\beta}^{n\rightarrow n'}(\mathbf{k}, \omega)$. We determined the most important interband transitions by means of their spectral weight within the chosen energy window.

In Fig. 4, we present the results of this analysis for $\mathrm{Re}\,\sigma_{xx}$ and $\mathrm{Im}\,\sigma_{xy}$ in the photon energy window $\hbar\omega = 0$–0.25 eV, corresponding to experimental features 1 and 2 in Fig. 2. Three transitions (between the bands $2 \rightarrow 3$, $3 \rightarrow 4$, and $4 \rightarrow 6$) reproduce the total spectra within this energy window almost perfectly. Looking at the individual transitions in Figs. 4(b)–4(e) reveals that the low-energy peak in $\mathrm{Re}\,\sigma_{xx}$ is partially formed by transitions close to the K point ($2 \rightarrow 3$, $3 \rightarrow 4$), i.e., hot spots of the spectral density trace a double helix in k space. This resembles the shape of two gapped helical nodal lines formed by bands 2 and 3 and traveling along the H'-K-H'' line, similar to the structures found in Ref. [30]. For direct observation, Fig. S6 [40] compares the spectral density between bands 2 and 3 with their eigenvalue difference, yielding similar helical shapes.

The $\mathrm{Im}\,\sigma_{xy}$ spectrum is analyzed in a similar fashion in Figs. 4(f)–4(j). Note that for σ_{xy} negative contributions (colored blue in the Brillouin zone plots) can occur in the spectral density, arising from negative momentum matrix element products. The peak at 0.1 eV arises dominantly from transitions between bands $2 \rightarrow 3$ with the optical weight located around the K point in the same helical fashion as for $\mathrm{Re}\,\sigma_{xx}$. By contrast, the dip around 0.2 eV results from a transition located in the bulk of the Brillouin zone between bands $4 \rightarrow 6$ with a dominantly negative spectral density.

This analysis demonstrates the strength of magneto-optical spectroscopy in the investigation of low-energy topological electronic structures. While in the experimental $\mathrm{Re}\,\sigma_{xx}$ spectra, the low-energy peak (feature 1) is masked by the large Drude contribution, the low-energy interband transitions are clearly distinguished in σ_{xy} which enables direct experimental observation and grants valuable information way beyond the insights obtained from standard optical spectroscopy.

VI. CONCLUSIONS

In summary, our magneto-optical study of the low-energy excitations allowed us to identify the electronic structures responsible for the AHE in Fe_3Sn_2. In the optical Hall conductivity, we detected a series of spectral features, all of which give substantial contribution to the static AHE. We found that their signs are alternating, i.e., their contributions to the dc AHE compete with each other. These interband transitions fully determine the AHE at 100 K and above where the intrinsic AHE is dominant. In agreement with Ref. [30], our band and k-resolved calculation indicate helical electronic states emerging from the interplay of the spin-orbit coupling essential for topological semimetals and the inherent trigonal stacking of the kagome layers in Fe_3Sn_2. We found significant contributions to the low-energy σ_{xx} and σ_{xy} within these "helical volumes" in momentum space. Electronic states situated within this volume may form "helical" electronic liquids in the presence of electronic interactions, that are found to be important in the present case. In analogy to particle physics, low-energy Hamiltonians can mimic Dirac fermions with a defined helicity according to their momentum and spin. Consequently, also the helicity can serve as a quantum number at the Fermi level. While the spin degeneracy may be lifted by an external magnetic field, the degeneracy from helicity as a time-reversal invariant is preserved, resulting in a helical liquid. However, if this degeneracy is lifted in an interacting multiorbital system, with the Fermi energy intersecting only bands of one helicity, then the conduction modes will be formed by helical states whose spin is fixed by the propagation direction. The tunability of these states may be achieved by electric and/or magnetic fields making them highly relevant for spintronic applications.

Finally, we note that our magneto-optical approach is widely applicable for other materials, where the interplay of magnetism and electronic topology leads to a large AHE. Since these bulk measurements are sensitive to the position of the Fermi energy, they are also suitable to evaluate the effect of doping, which can serve as a tool to control the Hall response.

[1] Y. Xu, J. Zhao, C. Yi, Q. Wang, Q. Yin, Y. Wang, X. Hu, L. Wang, E. Liu, G. Xu, L. Lu, A. A. Soluyanov, H. Lei, Y. Shi, J. Luo, and Z. G. Chen, Electronic correlations and flattened band in magnetic Weyl semimetal candidate $Co_3Sn_2S_2$, Nat. Commun. **11**, 3985 (2020).

[2] J. X. Yin, S. S. Zhang, G. Chang, Q. Wang, S. S. Tsirkin, Z. Guguchia, B. Lian, H. Zhou, K. Jiang, I. Belopolski, N. Shumiya, D. Multer, M. Litskevich, T. A. Cochran, H. Lin, Z. Wang, T. Neupert, S. Jia, H. Lei, and M. Z. Hasan, Negative flat band magnetism in a spin-orbit-coupled correlated kagome magnet, Nat. Phys. **15**, 443 (2019).

[3] C. Mielke, Y. Qin, J.-X. Yin, H. Nakamura, D. Das, K. Guo, R. Khasanov, J. Chang, Z. Q. Wang, S. Jia, S. Nakatsuji, A. Amato, H. Luetkens, G. Xu, M. Z. Hasan, and Z. Guguchia, Nodeless kagome superconductivity in $LaRu_3Si_2$, Phys. Rev. Mater. **5**, 034803 (2021).

[4] M. Kang, L. Ye, S. Fang, J. S. You, A. Levitan, M. Han, J. I. Facio, C. Jozwiak, A. Bostwick, E. Rotenberg, M. K. Chan, R. D. McDonald, D. Graf, K. Kaznatcheev, E. Vescovo, D. C. Bell, E. Kaxiras, J. van den Brink, M. Richter, M. Prasad Ghimire *et al.*, Dirac fermions and flat bands in the ideal kagome metal FeSn, Nat. Mater. **19**, 163 (2020).

[5] L. Ye, M. Kang, J. Liu, F. von Cube, C. R. Wicker, T. Suzuki, C. Jozwiak, A. Bostwick, E. Rotenberg, D. C. Bell, L. Fu, R. Comin, and J. G. Checkelsky, Massive Dirac fermions in a ferromagnetic kagome metal, Nature (London) **555**, 638 (2018).

[6] N. P. Armitage, E. J. Mele, and A. Vishwanath, Weyl and Dirac semimetals in three-dimensional solids, Rev. Mod. Phys. **90**, 015001 (2018).

[7] Y. S. Dedkov, M. Holder, S. L. Molodtsov, and H. Rosner, Electronic structure of shandite $Co_3Sn_2S_2$, J. Phys.: Conf. Ser. **100**, 072011 (2008).

[8] S. S. Zhang, J. X. Yin, M. Ikhlas, H. J. Tien, R. Wang, N. Shumiya, G. Chang, S. S. Tsirkin, Y. Shi, C. Yi, Z. Guguchia, H. Li, W. Wang, T. R. Chang, Z. Wang, Y. F. Yang, T. Neupert, S. Nakatsuji, and M. Z. Hasan, Many-Body Resonance in a Correlated Topological Kagome Antiferromagnet, Phys. Rev. Lett. **125**, 046401 (2020).

[9] Z. Hou, W. Ren, B. Ding, G. Xu, Y. Wang, B. Yang, Q. Zhang, Y. Zhang, E. Liu, F. Xu, W. Wang, G. Wu, X. Zhang, B. Shen, and Z. Zhang, Observation of various and spontaneous magnetic skyrmionic bubbles at room temperature in a frustrated kagome magnet with uniaxial magnetic anisotropy, Adv. Mater. **29**, 1701144 (2017).

[10] M. Pereiro, D. Yudin, J. Chico, C. Etz, O. Eriksson, and A. Bergman, Topological excitations in a kagome magnet, Nat. Commun. **5**, 4815 (2014).

[11] Q. Yin, Z. Tu, C. Gong, Y. Fu, S. Yan, and H. Lei, Superconductivity and normal-state properties of kagome metal RbV_3Sb_5 single crystals, Chin. Phys. Lett. **38**, 037403 (2021).

[12] B. R. Ortiz, P. M. Sarte, E. M. Kenney, M. J. Graf, S. M. L. Teicher, R. Seshadri, and S. D. Wilson, Superconductivity in the $\mathbb{Z}_2$ kagome metal KV_3Sb_5, Phys. Rev. Mater. **5**, 034801 (2021).

[13] B. R. Ortiz, S. M. L. Teicher, Y. Hu, J. L. Zuo, P. M. Sarte, E. C. Schueller, A. M. Milinda Abeykoon, M. J. Krogstad, S. Rosenkranz, R. Osborn, R. Seshadri, L. Balents, J. He, and S. D. Wilson, CsV_3Sb_5: A Z_2 Topological Kagome Metal with a Superconducting Ground State, Phys. Rev. Lett. **125**, 247002 (2020).

[14] E. Uykur, B. R. Ortiz, O. Iakutkina, M. Wenzel, S. D. Wilson, M. Dressel, and A. A. Tsirlin, Low-energy optical properties of the nonmagnetic kagome metal CsV_3Sb_5, Phys. Rev. B **104**, 045130 (2021).

[15] E. Uykur, B. R. Ortiz, S. D. Wilson, M. Dressel, and A. A. Tsirlin, Optical detection of the density-wave instability in the kagome metal KV_3Sb_5, npj Quantum Mater. **7**, 16 (2022).

[16] N. Nagaosa, J. Sinova, S. Onoda, A. H. MacDonald, and N. P. Ong, Anomalous Hall effect, Rev. Mod. Phys. **82**, 1539 (2010).

[17] Z. Fang, N. Nagaosa, K. S. Takahashi, A. Asamitsu, R. Mathieu, T. Ogasawara, H. Yamada, M. Kawasaki, Y. Tokura, and K. Terakura, The anomalous Hall effect and magnetic monopoles in momentum space, Science **302**, 92 (2003).

[18] E. Liu, Y. Sun, N. Kumar, L. Muechler, A. Sun, L. Jiao, S. Y. Yang, D. Liu, A. Liang, Q. Xu, J. Kroder, V. Süß, H. Borrmann, C. Shekhar, Z. Wang, C. Xi, W. Wang, W. Schnelle, S. Wirth, Y. Chen *et al.*, Giant anomalous Hall effect in a ferromagnetic kagome-lattice semimetal, Nat. Phys. **14**, 1125 (2018).

[19] A. A. Burkov and L. Balents, Weyl Semimetal in a Topological Insulator Multilayer, Phys. Rev. Lett. **107**, 127205 (2011).

[20] Q. Wang, S. Sun, X. Zhang, F. Pang, and H. Lei, Anomalous Hall effect in a ferromagnetic Fe_3Sn_2 single crystal with a geometrically frustrated Fe bilayer kagome lattice, Phys. Rev. B **94**, 075135 (2016).

[21] A. Biswas, O. Iakutkina, Q. Wang, H. C. Lei, M. Dressel, and E. Uykur, Spin-Reorientation-Induced Band Gap in Fe_3Sn_2: Optical Signatures of Weyl nodes, Phys. Rev. Lett. **125**, 076403 (2020).

[22] J. X. Yin, S. S. Zhang, H. Li, K. Jiang, G. Chang, B. Zhang, B. Lian, C. Xiang, I. Belopolski, H. Zheng, T. A. Cochran, S. Y. Xu, G. Bian, K. Liu, T. R. Chang, H. Lin, Z. Y. Lu, Z. Wang, S. Jia, W. Wang *et al.*, Giant and anisotropic many-body spin-orbit tunability in a strongly correlated kagome magnet, Nature (London) **562**, 91 (2018).

[23] B. Malaman, G. Le Caer, and D. Fruchart, Magnetic properties of Fe_3Sn_2. II. Neutron diffraction study (and Mossbauer effect), J. Phys. F: Met. Phys. **8**, 2389 (1978).

[24] K. Heritage, B. Bryant, L. A. Fenner, A. S. Wills, G. Aeppli, and Y. A. Soh, Images of a first-order spin-reorientation phase transition in a metallic kagome ferromagnet, Adv. Funct. Mater. **30**, 1 (2020).

[25] L. A. Fenner, A. A. Dee, and A. S. Wills, Non-collinearity and spin frustration in the itinerant kagome ferromagnet Fe_3Sn_2, J. Phys.: Condens. Matter **21**, 452202 (2009).

[26] M. Altthaler, E. Lysne, E. Roede, L. Prodan, V. Tsurkan, M. A. Kassem, H. Nakamura, S. Krohns, I. Kézsmárki, and D. Meier, Magnetic and geometric control of spin textures in the itinerant kagome magnet Fe_3Sn_2, Phys. Rev. Res. **3**, 043191 (2021).

[27] M. Yao, H. Lee, N. Xu, Y. Wang, J. Ma, O. V. Yazyev, Y. Xiong, M. Shi, G. Aeppli, and Y. Soh, Switchable Weyl nodes in topological Kagome ferromagnet Fe_3Sn_2, arXiv:1810.01514.

[28] Z. Z. Lin and X. Chen, Tunable massive Dirac fermions in ferromagnetic Fe_3Sn_2 kagome lattice, Phys. Status Solidi RRL **14**, 1 (2020).

[29] H. Tanaka, Y. Fujisawa, K. Kuroda, R. Noguchi, S. Sakuragi, C. Bareille, B. Smith, C. Cacho, S. W. Jung, T. Muro, Y. Okada, and T. Kondo, Three-dimensional electronic structure in

ferromagnetic Fe_3Sn_2 with breathing kagome bilayers, Phys. Rev. B **101**, 161114(R) (2020).

[30] S. Fang, L. Ye, M. P. Ghimire, M. Kang, J. Liu, M. Han, L. Fu, M. Richter, J. van den Brink, E. Kaxiras, R. Comin, and J. G. Checkelsky, Ferromagnetic helical nodal line and Kane-Mele spin-orbit coupling in kagome metal Fe_3Sn_2, Phys. Rev. B **105**, 035107 (2022).

[31] Z. Lin, J. H. Choi, Q. Zhang, W. Qin, S. Yi, P. Wang, L. Li, Y. Wang, H. Zhang, Z. Sun, L. Wei, S. Zhang, T. Guo, Q. Lu, J. H. Cho, C. Zeng, and Z. Zhang, Flatbands and Emergent Ferromagnetic Ordering in Fe_3Sn_2 Kagome Lattices, Phys. Rev. Lett. **121**, 096401 (2018).

[32] S. Bordács, I. Kézsmárki, K. Ohgushi, and Y. Tokura, Experimental band structure of the nearly half-metallic $CuCr_2Se_4$: An optical and magneto-optical study, New J. Phys. **12**, 053039 (2010).

[33] R. Shimano, Y. Ikebe, K. S. Takahashi, M. Kawasaki, N. Nagaosa, and Y. Tokura, Terahertz Faraday rotation induced by an anomalous Hall effect in the itinerant ferromagnet $SrRuO_3$, Europhys. Lett. **95**, 17002 (2011).

[34] Y. Okamura, S. Minami, Y. Kato, Y. Fujishiro, Y. Kaneko, J. Ikeda, J. Muramoto, R. Kaneko, K. Ueda, V. Kocsis, N. Kanazawa, Y. Taguchi, T. Koretsune, K. Fujiwara, A. Tsukazaki, R. Arita, Y. Tokura, and Y. Takahashi, Giant magneto-optical responses in magnetic Weyl semimetal $Co_3Sn_2S_2$, Nat. Commun. **11**, 4619 (2020).

[35] R. O. Jones and O. Gunnarsson, The density functional formalism, its applications and prospects, Rev. Mod. Phys. **61**, 689 (1989).

[36] W. Kohn, Nobel lecture: Electronic structure of matter wave functions and density functionals, Rev. Mod. Phys. **71**, 1253 (1999).

[37] R. O. Jones, Density functional theory: Its origins, rise to prominence, and future, Rev. Mod. Phys. **87**, 897 (2015).

[38] M. Z. Hasan and C. L. Kane, Colloquium: Topological insulators, Rev. Mod. Phys. **82**, 3045 (2010).

[39] D. Xiao, M.-C. Chang, and Q. Niu, Berry phase effects on electronic properties, Rev. Mod. Phys. **82**, 1959 (2010).

[40] See Supplemental Material at http://link.aps.org/supplemental/10.1103/PhysRevB.106.144404 for the reflectivity and MOKE spectra together with the dc AHE data and details of the crystal growth, which includes Refs. [46–50].

[41] H. Feil and C. Haas, Magneto-Optical Kerr Effect, Enhanced by the Plasma Resonance of Charge Carriers, Phys. Rev. Lett. **58**, 65 (1987).

[42] P. Blaha, K. Schwarz, G. K. H. Madsen, D. Kvasnicka, J. Luitz, R. Laskowski, F. Tran, and L. D. Marks, *WIEN2k, An Augmented Plane Wave + Local Orbitals Program for Calculating Crystal Properties* (Karlheinz Schwarz, Techn. Universität Wien, Austria, 2018).

[43] J. P. Perdew, K. Burke, and M. Ernzerhof, Generalized Gradient Approximation Made Simple, Phys. Rev. Lett. **77**, 3865 (1996).

[44] S. A. Ekahana, Y. Soh, A. Tamai, D. Gosálbez-Martinez, M. Yao, A. Hunter, W. Fan, Y. Wang, J. Li, A. Kleibert, C. A. F. Vaz, J. Ma, Y. Xiong, O. V. Yazyev, F. Baumberger, M. Shi, and G. Aeppli, Anomalous quasiparticles in the zone center electron pocket of the kagomé ferromagnet Fe_3Sn_2, arXiv:2206.13750.

[45] R. Kubo, Statistical-mechanical theory of irreversible processes. I. General theory and simple applications to magnetic and conduction problems, J. Phys. Soc. Jpn. **12**, 570 (1957).

[46] D. B. Tanner, Use of x-ray scattering functions in Kramers-Kronig analysis of reflectance, Phys. Rev. B **91**, 035123 (2015).

[47] K. Sato, Measurement of magneto-optical Kerr effect using piezo-birefringent modulator, Jpn. J. Appl. Phys. **20**, 2403 (1981).

[48] L. Demkó, G. A. H. Schober, V. Kocsis, M. S. Bahramy, H. Murakawa, J. S. Lee, I. Kézsmárki, R. Arita, N. Nagaosa, and Y. Tokura, Enhanced Infrared Magneto-Optical Response of the Nonmagnetic Semiconductor BiTeI Driven by Bulk Rashba Splitting, Phys. Rev. Lett. **109**, 167401 (2012).

[49] A. B. Kuzmenko, Kramers-Kronig constrained variational analysis of optical spectra, Rev. Sci. Instrum. **76**, 083108 (2005).

[50] C. Ambrosch-Draxl and J. O. Sofo, Linear optical properties of solids within the full-potential linearized augmented planewave method, Comput. Phys. Commun. **175**, 1 (2006).